

Microwave Meissner Screening Properties of Proximity coupled Topological Insulator / Superconductor Bilayers

Seokjin Bae,¹ Seunghun Lee,^{1,2} Xiaohang Zhang,^{1,2} Ichiro Takeuchi,^{1,2} and Steven M. Anlage¹

¹*Center for Nanophysics and Advanced Materials, Department of Physics,
University of Maryland, College Park, MD 20742, USA*

²*Department of Materials Science and Engineering,
University of Maryland, College Park, Maryland 20742, USA*

(Dated: August 4, 2021)

The proximity coupled topological insulator / superconductor (TI/SC) bilayer system is a representative system to realize topological superconductivity. In order to better understand this unique state and design devices from the TI/SC bilayer, a comprehensive understanding of the microscopic properties of the bilayer is required. In this work, a microwave Meissner screening study, which exploits a high-precision microwave resonator technique, is conducted on the SmB₆/YB₆ thin film bilayers as an example TI/SC system. The study reveals spatially dependent electrodynamic screening response of the TI/SC system that is not accessible to other techniques, from which the corresponding microscopic properties of a TI/SC bilayer can be obtained. The TI thickness dependence of the effective penetration depth suggests the existence of a bulk insulating region in the TI layer. The spatially dependent electrodynamic screening model analysis provides an estimate for the characteristic lengths of the TI/SC bilayer: normal coherence length, normal penetration depth, and the thickness of the surface states. We also discuss implications of these characteristic lengths on the design of a vortex Majorana device such as the radius of the vortex core, the energy splitting due to intervortex tunneling, and the minimum thickness required for a device.

I. INTRODUCTION

Creating an experimental platform which hosts Majorana bound states (MBSs) in a condensed matter system is a goal that has received great attention recently.^{1,2} Due to robust topological protection, the MBS is a promising qubit candidate for quantum computation.³ One of the platforms proposed to realize the MBS is a topological insulator / superconductor (TI/SC) bilayer system.⁴ With the induced chiral p -wave superconductivity in the topological surface states (TSS), an MBS has been predicted to exist in its vortex core.^{5–8} Therefore, it is important for the physics community to establish and understand the properties of TI/SC bilayer systems.

There have been a number of studies on the Bi-based TI (Bi₂Se₃, Bi₂Te₃, etc) /SC systems through point contact spectroscopy (PCS),⁹ ARPES,^{10,11} and STM^{12–14} measurements. PCS and STM probe the magnitude of the superconducting order parameter induced in the top surface of the TI with a probing depth range limited to the mean free path or coherence length, and cannot be applied to the case when an insulating bulk region is present. ARPES studies the angle-resolved magnitude of the induced order parameter from the first few atomic layers of the top surface of the TI.

In contrast, a microwave Meissner screening study investigates the high frequency electromagnetic field response. The microwave field propagates through an insulating layer and penetrates inside the superconducting system to the scale of the penetration depth, which is comparable to the thickness of typical thin-film bilayers (< 200 nm). Since the field screening response arises throughout the entire bilayer, it can reveal more details of the proximity-coupled bilayer^{15–19} that are not directly

available to the other techniques. It is also important to note that the screening response study does not require specialized surface preparation which is critical for many of the other techniques.

The distinct capabilities of the Meissner screening study on the proximity-coupled system have been previously demonstrated on conventional normal (N) / superconductor (S) bilayer systems such as Cu (N) / Nb (S).^{16,20–28} It can reveal the spatial distribution of the order parameter and the magnetic field profile throughout the film, as well as their evolution with temperature. From such information, superconducting characteristic lengths such as the normal coherence length ξ_N and normal penetration depth λ_N of the proximity-coupled normal layer can be estimated. The study can also reveal thickness dependent proximity-coupling behavior, which helps to estimate the thickness of the surface states (t_{TSS}) for TI/SC bilayers. The ξ_N , λ_N , and t_{TSS} of a proximity-coupled TI layer determine the radius of a vortex, the maximum spacing between vortices in a lattice, and the minimum thickness of the TI layer. Such information is required to avoid intervortex tunneling of MBSs, which would result in a trivial fermionic state.²⁹

Compared to other high frequency electromagnetic techniques such as THz optical measurement, the advantage of the microwave Meissner screening study for investigating the properties of a TI/SC bilayer is that the energy of a 1 GHz microwave photon ($\approx 4 \mu\text{eV}$) is a marginal perturbation to the system. On the other hand, the energy of a 1 THz optical photon ($\approx 4 \text{meV}$) is comparable to the gap energy ($\leq 3 \text{meV}$) of typical superconductors used in TI/SC systems such as Nb, Pb, Al, NbSe₂, and YB₆.^{30–32} Therefore, the microwave screening study is an ideal method to study details of the in-

duced order parameter in TI/SC bilayers.

In this article, we conduct a microwave Meissner screening study on SmB_6/YB_6 : a strong candidate for topological Kondo insulator / superconductor bilayer systems. The existence of the insulating bulk in SmB_6 is currently under debate.^{33–40} From measurements of the temperature dependence of the Meissner screening with a systematic variation of SmB_6 thickness, this study shows evidence for the presence of an insulating bulk region in the SmB_6 thin films. Through a model of the electrodynamics, the study also provides an estimation for the characteristic lengths of the bilayer system including the thickness of the surface states.

II. EXPERIMENT

SmB_6/YB_6 bilayers were fabricated through a sequential sputtering process without breaking the vacuum to ensure a pristine interface between SmB_6 and YB_6 for ideal proximity coupling. The details of sample fabrication can be found in the Appendix Sec. A 1. The geometry of the bilayers is schematically shown in Fig. 1(a). The YB_6 film has a thickness of 100 nm and $T_c = 6.1$ K obtained from a DC resistance measurement.⁴¹ The thickness of SmB_6 layers (t_{SmB_6}) are varied from 20 to 100 nm for systematic study. These bilayers all have $T_c = 5.8 \pm 0.1$ K without a noticeable t_{SmB_6} dependence of T_c . The measurement of the effective penetration depth λ_{eff} is conducted with a dielectric resonator setup.^{42–44} A 3 mm diameter, 2 mm thick rutile (TiO_2) disk, which facilitates a microwave transmission resonance at 11 GHz, is placed on top of the sample mounted in a Hakki-Coleman type resonator.⁴² This resonator consists of niobium (top) and copper (bottom) plates to obtain a high quality factor for the dielectric resonance. The resonator is cooled down to the base temperature of 40 mK. As the temperature of the sample is increased from the base temperature, the change of the resonance frequency is measured, $\Delta f_0(T) = f_0(T) - f_0(T_{ref})$. T_{ref} here is set to 230 mK ($\approx 0.04T_c$ of the bilayers), below which $f_0(T)$ of the bilayers shows saturated temperature dependence. This data is converted to the change in the effective penetration depth $\Delta\lambda_{eff}(T)$ using a standard cavity perturbation theory,^{45–47}

$$\Delta\lambda_{eff}(T) = \lambda_{eff}(T) - \lambda_{eff}(T_{ref}) = -\frac{G_{geo}}{\pi\mu_0} \frac{\Delta f_0(T)}{f_0^2(T)}. \quad (1)$$

Here, G_{geo} is the geometric factor of the resonator.⁴⁴

Fig. 1(b) shows $\Delta\lambda_{eff}(T)$ for the SmB_6 (N) / YB_6 (S) bilayers for various SmB_6 layer thickness t_{SmB_6} . The single layer YB_6 thin film (i.e., $t_{\text{SmB}_6} = 0$) shows temperature independent behavior below $T/T_c < 0.2$. This is not only consistent with the BCS temperature dependence of $\Delta\lambda(T)$ for a spatially homogeneous, fully-gapped superconductor,^{48,49} but also consistent with previous observations on YB_6 single crystals.^{32,50} However,

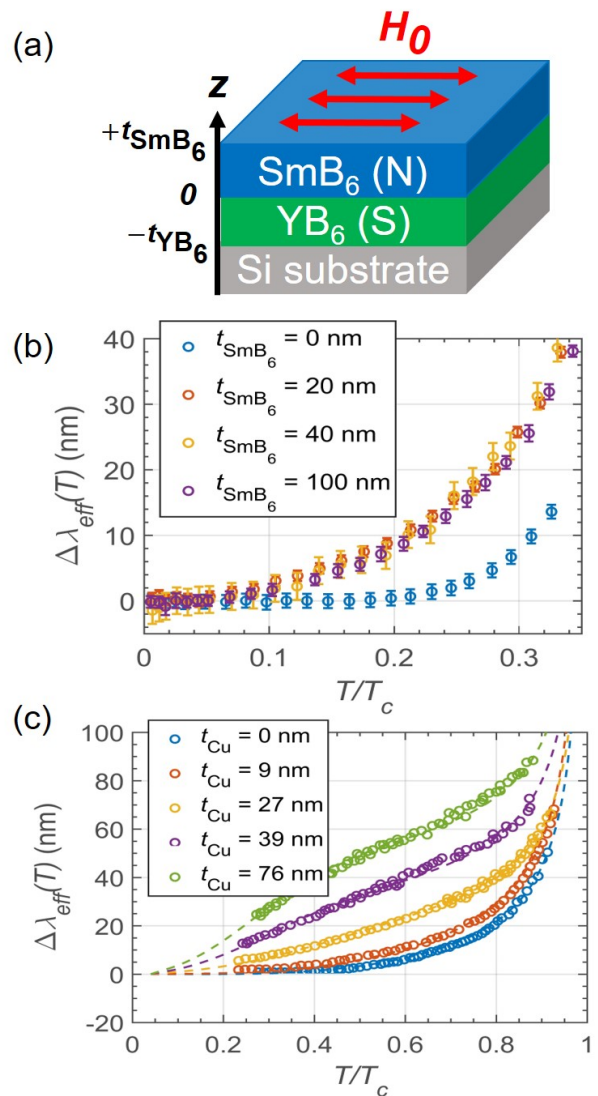


FIG. 1. (a) A schematic of the bilayer consisting of an SmB_6 film and a YB_6 film. A parallel microwave magnetic field (H_0) is applied to the top surface of the SmB_6 layer (red arrows). (b) Temperature dependence of the effective penetration depth $\Delta\lambda_{eff}(T)$ of the SmB_6/YB_6 bilayers for various SmB_6 layer thickness (t_{SmB_6}). (c) $\Delta\lambda_{eff}(T)$ of a Cu/Nb (conventional metal / superconductor) bilayers²⁷ for various Cu layer thickness (t_{Cu}). The dashed lines are the model fits.²⁷

once the SmB_6 layer is added, $\Delta\lambda_{eff}(T)$ clearly shows temperature dependence below $T/T_c < 0.2$. Here, the important unconventional feature is that the low temperature profile of $\Delta\lambda_{eff}(T)$ for the SmB_6/YB_6 bilayers shows only a marginal t_{SmB_6} dependence. This is in clear contrast to the case of the Cu (N) / Nb (S) bilayers shown in Fig. 1(c). The $\Delta\lambda_{eff}(T)$ for this conventional metal/superconductor bilayer system shows considerable evolution as the normal layer thickness t_{Cu} increases. This is because when the decay length of the induced order parameter $\xi_N(T)$ decreases with increasing temperature, the thicker (thinner) normal layer undergoes

a larger (smaller) change in the spatial distribution of the order parameter, and hence the spatial profile of the screening. Therefore, the marginal t_{SmB_6} dependence of $\Delta\lambda_{eff}(T)$ for the SmB₆/YB₆ bilayer implies that even though t_{SmB_6} is increased, the actual thickness of the proximity-coupled screening region in the SmB₆ layer remains roughly constant.

III. MODEL

To quantitatively analyze this unconventional behavior, an electromagnetic screening model for a proximity-coupled bilayer is introduced.^{16,25,27,28} The model solves Maxwell's equations combined with the second London equation for the current and field inside the bilayer with appropriate boundary conditions at each temperature (See Appendix D), to obtain the spatial profile of the magnetic field $H(z, T)$ and the current density $J(z, T)$ as a function of temperature,¹⁶ where z denotes the coordinate along the sample thickness direction as depicted in Fig. 1(a). From the obtained field and current profiles, one can obtain the total inductance $L(T)$ of the bilayer as

$$L(T) = \frac{\mu_0}{H_0^2} \int_{-t_S}^0 [H^2(z, T) + \lambda_S^2(T)J^2(z, T)] dz + \frac{\mu_0}{H_0^2} \int_0^{+d_N} [H^2(z, T) + \lambda_N^2(z, T)J^2(z, T)] dz + \frac{\mu_0}{H_0^2} \int_{+d_N}^{+t_N} [H^2(z)] dz, \quad (2)$$

from which one can obtain an effective penetration depth from the relation $L(T) = \mu_0\lambda_{eff}(T)$. Here, H_0 is the amplitude of the applied microwave magnetic field at the top surface of the normal layer (see Fig. 1(a)), λ_S (λ_N) is local penetration depth of the superconductor (normal layer), t_S is the thickness of the superconductor, t_N ($N=\text{SmB}_6$ or Cu) is the total thickness of the normal layer, and d_N ($\leq t_N$, integration limit of the second and third terms in Eq. (2)) is the thickness of the proximity-coupled region in the normal layer, which is assumed to be temperature independent. In Eq.(2), H^2 is proportional to field stored energy and $\lambda^2 J^2$ is proportional to kinetic stored energy of the supercurrent. The first, second, and third integration terms come from the superconductor, the proximity-coupled part of the normal layer, and the uncoupled part of the normal layer, respectively.

A schematic view of the order parameter profile in the bilayers is shown in Fig. 2. As seen in Fig. 2(a), for a conventional metal, d_N is the same as t_N since the entire normal layer is uniformly susceptible to induced superconductivity, and thus the third integration term in Eq. 2 becomes zero. However, as seen in Fig. 2(b), if there exists an insulating bulk region blocking the propagation of the order parameter up to the top surface in the normal layer (as in the case of a thick TI), only the

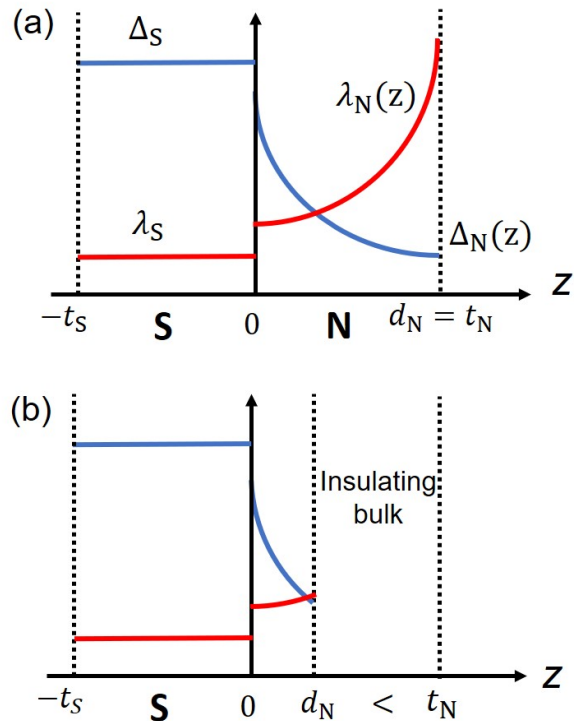


FIG. 2. (a) Schematic spatial profile of the order parameter $\Delta_{N,S}$ (blue) and the local penetration depth $\lambda_{N,S}$ (red) through the normal layer (N) / superconductor (S) bilayer sample for the case of the absence of an insulating bulk. z is the thickness direction coordinate and t_N (t_S) is the thickness of the normal layer (superconductor). The proximitized thickness d_N is equal to the normal layer thickness t_N . (b) In the presence of an insulating bulk, $d_N < t_N$ since the insulating bulk blocks propagation of the order parameter to the top surface. Note that the microwave magnetic field is applied to the right surfaces.

bottom conducting surface adjacent to the superconductor is proximity-coupled. In this case, d_N becomes the thickness of the bottom conducting surface states. The third integration term in Eq. (2), which accounts for the uncoupled portion of the normal layer, becomes non-zero. However, this third term can be removed by taking $\Delta L(T)$ into account since the uncoupled SmB₆ region has temperature-independent microwave properties below 3 K,⁵¹ whereas the temperature range of the measurement here extends below 2 K.

The spatial dependence of screening of the proximity-coupled normal layer is imposed by that of the induced order parameter Δ_N (Fig. 2(a)), which can be approximated by an exponential decay profile $\Delta_N(z, T) = \Delta_N(0, T)e^{-z/\xi_N(T)}$ in terms of the normal coherence length $\xi_N(T)$.¹⁸ The position dependent normal penetration depth is inversely proportional to the order parameter $\lambda_N \sim 1/\Delta_N$ ⁵² so its position dependence is expressed as $\lambda_N(z, T) = \lambda_N(0, T)e^{z/\xi_N(T)}$. Here, the temperature dependence of λ_N at the interface is assumed to

follow that of the superconductor⁵³ $\lambda_N(0, T)/\lambda_N(0, 0) = \lambda_S(T)/\lambda_S(0) \cong 1 + \sqrt{\pi}\Delta_0/2k_B T \exp(-\Delta_0/k_B T)$, which is the asymptotic behavior below $0.3T_c$ for a fully-gapped superconductor.^{48,49}

For the temperature dependence of the screening in the normal layer, $\xi_N(T)$ plays a crucial role since it determines the spatial distribution of $\Delta_N(z, T)$. If the sample is in the clean limit, the temperature dependence of the normal coherence length is given by $\xi_N = \hbar v_F/2\pi k_B T$, where v_F denotes the Fermi velocity of the N layer. In the dirty limit, it is given by $\xi_N = \sqrt{\hbar v_F l_N/6\pi k_B T}$,¹⁵ where l_N denotes the mean-free path of the N layer. For the model fitting, the simplified expressions $\xi_N^{clean}(T) = \xi_N^{clean}(T_0) \times T_0/T$ and $\xi_N^{dirty}(T) = \xi_N^{dirty}(T_0) \times \sqrt{T_0/T}$ are used, with $\xi_N(T_0)$ as a fitting parameter. Here, T_0 is an arbitrary reference temperature of interest. Note that the divergence of $\xi_N(T)$ as $T \rightarrow 0$ should be cut off below a saturation temperature due to the finite thickness of the normal layer, which is theoretically predicted,^{15,54} and also experimentally observed from magnetization studies on other bilayer systems.^{23,26} In our measurements, the effect of this saturation of $\xi_N(T)$ can be seen from the sudden saturation of the $\Delta\lambda_{eff}(T)$ data below $0.04T_c$ (see Fig. 1(b) and Fig. 3(b-d)). Therefore, only the data obtained in a temperature range of $T/T_c \geq 0.04$ is fitted, where the $\Delta\lambda_{eff}(T)$ data indicates that ξ_N is temperature dependent.

A given set of these parameters $\lambda_S(0)$, $\lambda_N(0, 0)$, $\xi_N(T_0)$, and d_N determines a model curve of $\Delta\lambda_{eff}(T)$. Therefore, by fitting the experimental data to a model curve, one can determine the values of these characteristic lengths. This screening model has successfully described $\Delta\lambda(T)$ behavior of various kinds of normal/superconductor bilayers.^{25,27,28}

IV. RESULTS

As seen in Fig. 3(a), the model is first applied to fit $\Delta\lambda_{eff}(T)$ of a single layer YB₆ thin film (i.e., no SmB₆ layer on the top) to obtain $\lambda_S(0)$: the simplest case where one needs to consider only the first term in Eq. (2). Here, the data in a temperature range of $T < 1.6$ K ($\approx 0.28T_c$ of the SmB₆/YB₆ bilayers) is fitted to avoid the contribution from the niobium top plate to $\Delta f_0(T)$. The best fit is determined by finding the fitting parameters that minimize the root-mean-square error σ of $\Delta\lambda_{eff}(T)$ between the experimental data and the model fit curves. The best fit gives $\lambda_S(0) = 227 \pm 2$ nm (The determination of the error bar is described in Appendix C 2). A comparison between the estimated $\lambda_S(0)$ of the YB₆ thin film and that obtained in other work is discussed in the Appendix A 2

We now fix the value of $\lambda_S(0)$ of the YB₆ layer and focus on extracting the characteristic lengths of the induced superconductivity of the bilayers. Recent PCS measurements on a series of SmB₆/YB₆ bilayers⁴¹ help to reduce the number of fitting parameters: the point contact

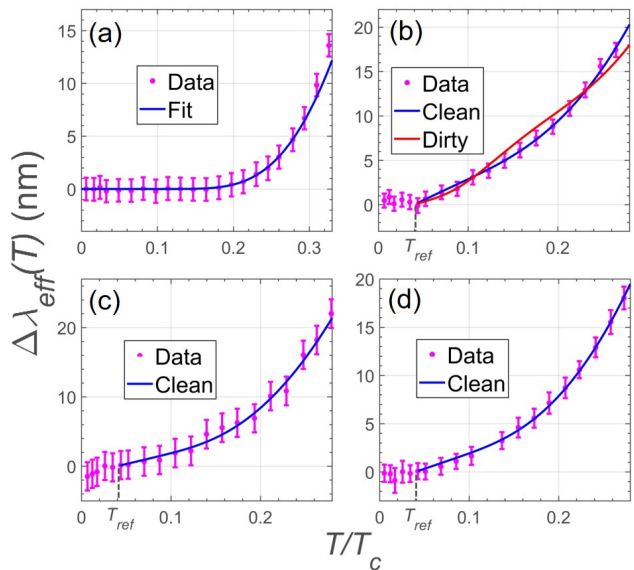


FIG. 3. $\Delta\lambda_{eff}(T)$ vs. T/T_c data and fits for SmB₆/YB₆ bilayers at low temperature, $T/T_c < 0.3$. (a) The single layer YB₆ (100 nm) ($t_{SmB_6} = 0$ nm). The magenta points are data, and the blue line is a fit from the electromagnetic screening model. (b) The bilayer with $t_{SmB_6} = 20$ nm. The blue line is a fit with the clean limit temperature dependence of $\xi_N(T)$, and the red line is a fit with the dirty limit temperature dependence. (c) and (d) The bilayers with $t_{SmB_6} = 40$ nm and 100 nm, respectively.

measurement on the bilayer with $t_{SmB_6} = 20$ nm at 2 K showed perfect Andreev reflection, i.e., conductance doubling at the interface between a metal tip and the top surface of the SmB₆, indicating that the entire 20 nm thick SmB₆ layer is proximity-coupled. Therefore, d_N is fixed to 20 nm when fitting the $\Delta\lambda_{eff}(T)$ data of the bilayer with $t_{SmB_6} = 20$ nm.

The fitting is conducted with the clean and the dirty limit temperature dependence of $\xi_N(T)$ as shown in Fig. 3(b). The clean limit fit (blue) gives $\xi_N^{clean}(2K) = 52 \pm 1$ nm, $\lambda_N(0, 0) = 340 \pm 2$ nm with σ of 0.237. On the other hand, the dirty limit fit (red) gives $\xi_N^{dirty}(2K) = 262 \pm 180$ nm, $\lambda_N(0, 0) = 505 \pm 7$ nm with σ of 0.780. According to the fitting result, not only does the dirty limit fit apparently deviate from the data points, but also the σ of the dirty limit is three times larger than that of the clean limit, implying that the clean limit is more appropriate for describing $\xi_N(T)$ of the SmB₆ layer. Henceforth, the $\Delta\lambda_{eff}(T)$ data for the bilayers with other t_{SmB_6} is fit using the clean limit temperature dependence of ξ_N . Also, the obtained value of $\xi_N(2K) = 52$ nm will be used when the data of the bilayers with other t_{SmB_6} is fitted, as the Fermi velocity of the surface bands, which determines the value of ξ_N , does not have a clear TI layer thickness dependence.¹¹

For the bilayers with $t_{SmB_6} = 40$ and 100 nm, d_N is now set to be a free fitting parameter. As seen from Fig. 3(c) and (d), the resulting fit line gives $d_N = 8 \pm 2$ nm,

Characteristic lengths	SmB ₆ layer thickness		
	20 nm	40 nm	100 nm
$\xi_N(2K)$ (nm)	52 ± 1	52^*	52^*
d_N (nm)	20^*	8 ± 2	10 ± 1
$\lambda_N(0, 0)$ (nm)	340 ± 2	159 ± 2	207 ± 2

TABLE I. Summary of the extracted characteristic lengths from the electrodynamic screening model for TI/SC bilayers for different SmB₆ layer thickness. All fits on the bilayers assume $\lambda_S(0) = 227$ nm which is obtained from the fitting on the single layer YB₆. Note that the values with the asterisk are fixed when the fitting is conducted.

$\lambda_N(0, 0) = 159 \pm 2$ nm for the bilayer with $t_{\text{SmB}_6} = 40$ nm, and $d_N = 10 \pm 1$ nm, $\lambda_N(0, 0) = 207 \pm 2$ nm for the bilayer with $t_{\text{SmB}_6} = 100$ nm. The estimated $d_N \approx 9$ nm is much smaller than t_{SmB_6} , which is consistent with the absence of induced order parameter in the top surface of 40 and 100 nm thick SmB₆ layers measured by point contact spectroscopy.⁴¹ A summary of the estimated characteristic lengths $\xi_N(2K)$, d_N , and $\lambda_N(0, 0)$ for the case of 20, 40, and 100 nm thick SmB₆ layers on top of YB₆ is presented in Table. I.

V. DISCUSSION

We now discuss the implications of these results and propose a microscopic picture for the proximity coupled bilayers. The important implication of the above results is the absence of Meissner screening in the bulk of proximity-coupled SmB₆, which is consistent with the existence of an insulating bulk region inside the SmB₆ layer. If the entire SmB₆ layer is conducting without an insulating bulk inside, the proximity-coupled thickness d_N should be equal to t_{SmB_6} for thicker films too, considering the long normal coherence length of ≈ 52 nm. In that case, as t_{SmB_6} increases, one would expect a continuous evolution of stronger $\Delta\lambda(T)$ as seen in the Cu/Nb system (Fig. 1(c)), which is not observed in Fig. 1(b). Also, the estimated $d_N \approx 9$ nm for the bilayers with $t_{\text{SmB}_6} = 40$ and 100 nm is much smaller than half of t_{SmB_6} . As illustrated in Fig. 4(a), this situation can only be explained if a thick insulating bulk region of $t_{\text{bulk}} \approx 22$ and 82 nm exist in the bilayers with $t_{\text{SmB}_6} = 40$ and 100 nm respectively.

This thick insulating bulk provides a spatial separation between the top and bottom surface conducting states, not allowing the order parameter to propagate to the top surface. Thus, only the bottom surface states are proximitized in the $t_{\text{SmB}_6} = 40$ and 100 nm cases, and hence one can conclude that the proximitized thickness $d_N \approx 9$ nm equals the thickness of the surface states t_{TSS} . Note that this confirmation of the presence of the insulating bulk in the TI layer cannot be made solely from the PCS study. Even if the PCS study observed the absence of the order parameter on the top surface of the TI layer (SmB₆ in this case), it could be either due

to an insulating bulk, or due to a short normal coherence length $\xi_N < t_{\text{SmB}_6}$. The large value of $\xi_N = 52$ nm, which is larger than $t_{\text{SmB}_6} = 40$ nm, rules out the latter scenario and confirms the presence of an insulating bulk inside the SmB₆ layers.

This picture is also consistent with the observation that the entire SmB₆ layer with $t_{\text{SmB}_6} = 20$ nm is proximity-coupled (Fig. 4(b)); the top and the bottom conducting surface state wavefunctions are likely to be weakly overlapped based on $2t_{\text{TSS}} \approx t_{\text{SmB}_6}$ through the exponentially decaying profile (Fig. 4(b)). Thus the induced order parameter is able to reach to the top surface states, giving $d_N = 20$ nm for this case. Although such overlap is expected to open a hybridization gap in the surface states, the fact that 20 nm SmB₆ on YB₆ is entirely proximity-coupled implies that the opened gap is much smaller than the energy difference between the Fermi level of SmB₆ and the Dirac point. Note that topological protection might not be affected by such weak hybridization, provided that the Fermi level is sufficiently far away from the Dirac point present in thick SmB₆.¹¹

Besides confirming the existence of an insulating bulk in the SmB₆ layer, the extracted fitting parameters based on the electromagnetic model provide an estimate for the important characteristic lengths such as ξ_N , λ_N , and t_{TSS} , as seen from Sec. IV. These estimates can be utilized in designing a TI/SC device such as a vortex MBS device. ξ_N determines the radius of the vortex core r_v . In the mixed state above the first critical field, λ_N determines the maximum spacing R_v between neighboring vortices in the vortex lattice.⁵⁵ The ratio r_v/R_v determines the overlap of the two adjacent MBSs. The overlap of the wavefunctions of the two MBSs results in intervortex tunneling, which splits the energy level of the MBSs away from the zero energy and make them trivial fermionic excitations,²⁹

$$\Delta E_{\text{split}} \sim \frac{1}{\sqrt{k_F R_v(\lambda_N)}} \exp\left(-\frac{R_v(\lambda_N)}{r_v(\xi_N)}\right). \quad (3)$$

Therefore, information on ξ_N and λ_N helps to evaluate how secure the MBSs of a device will be against the intervortex tunneling.

t_{TSS} determines a minimum required thickness of the device. If the thickness of the device is too thin ($t_{\text{SmB}_6} \sim t_{\text{TSS}}$), the wavefunction overlap between the top and bottom surface states becomes significant, which opens a large hybridization gap up to the Fermi level. As a result, the surface states lose not only the electric conduction but also lose the spin-momentum locking property.¹¹ In this case, MBS is not hosted in the vortex core, and hence a thickness larger than the estimated $2t_{\text{TSS}}$ is recommended. These discussions show how the characteristic lengths extracted from the Meissner screening study serve as a guideline to design a vortex MBS device with TI/SC bilayer systems.

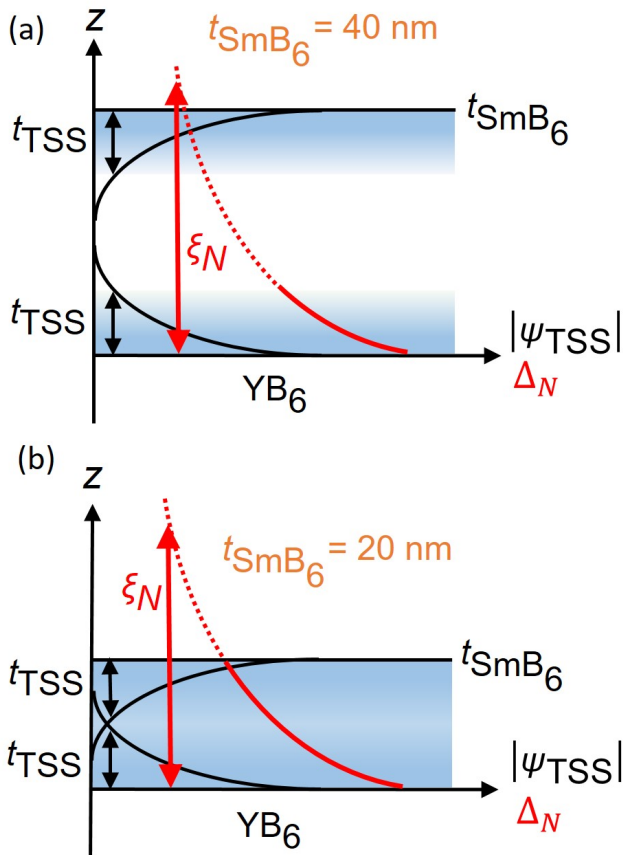


FIG. 4. Schematic view (not to scale) of the proposed position dependence of the surface states wavefunction $|\psi_{\text{TSS}}(z)|$ (black) and induced order parameter $\Delta_N(z)$ (red) in the SmB_6/YB_6 bilayer. The $|\psi_{\text{TSS}}(z)|$ is also visualized by the blue gradations. The sketches are based on the estimated proximity-coupled thickness $d_N \approx 9$ nm and the normal coherence length $\xi_N(2\text{K}) = 52$ nm for the case of $t_{\text{SmB}_6} =$ (a) 40 nm, and (b) 20 nm.

VI. CONCLUSION

In summary, a microwave Meissner screening study is introduced and utilized to investigate the spatially dependent electrodynamic screening response and the corresponding properties of the TI/SC bilayers. The advantages of the study in investigating the properties of a TI/SC system is demonstrated by the measurement and modeling of the temperature dependence of the screening with systematic TI-layer thickness variation. The study goes beyond the surface response to examine the screening properties of the entire TI layer, and uncovers the existence of an insulating bulk in the TI layer conclusively. Also, the study provides an estimate for characteristic lengths of the TI/SC bilayer, which sheds light on the design of a vortex MBS device providing guidelines for the radius of the vortex core, the energy level splitting due to the intervortex tunneling, and the thickness of the device. With its versatile capabilities, the microwave

Meissner screening study can serve as a standard characterization method for a variety of TI/SC systems before using them as building blocks in topological quantum computation.

ACKNOWLEDGMENTS

The authors thank Yun-Suk Eo and Valentin Stanev for helpful discussions. This work is supported by NSF grant No. DMR-1410712, DOE Office of High Energy Physics under Award No. DE-SC 0012036T (support of S.B.), Office of Basic Energy Science, Division of Material Science and Engineering under Award No. DE-SC 0018788 (measurements), ONR grant No. N00014-13-1-0635, AFOSR grant No. FA 9550-14-10332 (support of S.L., X.Z., and I.T.), and the Maryland Center for Nanophysics and Advanced Materials.

Appendix A: Sample properties

1. Thin film bilayer preparation

SmB_6/YB_6 bilayers were prepared by an in-situ sequential sputtering process (i.e., without breaking vacuum) to secure the ideal superconducting proximity effect which is a prerequisite for the current study and analyses.⁵⁶ SmB_6 and YB_6 share the same crystal structure with almost the same lattice constant (≈ 4.1 Å), which allows the fabrication of bilayers by sequential high-temperature growth under the same conditions. YB_6 is a superconducting rare-earth hexaboride and it has been reported that slight boron deficiency improves the superconducting transition temperature (T_c) of YB_6 .⁴¹ Thus, for this study, slightly boron deficient YB_6 films (B/Y = 5.6) were used as the superconducting layers. YB_6 thin films were deposited on Si(001) substrates. To remove the native oxide layer on the Si substrate, we treated it with hydrofluoric acid (HF) before the thin film deposition. The base pressure of the deposition system was 2×10^{-8} Torr. The deposition process was performed at 860 °C under a pressure of 10 mTorr adjusted by Ar gas (99.999 %). The thickness of YB_6 layers was fixed to be 100 nm. The subsequent SmB_6 deposition was performed under the same temperature and pressure conditions, and an additional sputtering of B target was employed to compensate B deficiency which is present in the films fabricated by the sputtering of a stoichiometric SmB_6 target.^{56,57} The compositions (i.e., stoichiometry) of YB_6 and SmB_6 thin films were examined with wavelength dispersive spectroscopy (WDS) measurements. The thicknesses of bilayers were confirmed with cross-sectional scanning electron microscopy (SEM) measurements.

	This work	previous work
$\xi_N(2K)$ (nm)	52 (clean limit)	9^{56} (dirty limit)
v_F (10^4 m/s)	8.5	$4^{62,63}$ (ARPES) 9^{56} (transport) 0.6^{59} (STM) 0.4^{64} (theory)
t_{TSS} (nm)	≈ 9	6^{56} (transport) 32^{65} (spin pumping)

TABLE II. Characteristic lengths (ξ_N and t_{TSS}) of the SmB₆/YB₆ bilayers and derived property (v_F) for SmB₆ obtained from the microwave Meissner screening study compared to those from previous studies.

2. Validity of the estimated magnetic penetration depth of the YB₆ thin film

In the main text (Fig. 2(a)), the model fit gives $\lambda_S(0) = 227 \pm 2$ nm (and $2\Delta(0)/k_B T_c = 3.66 \pm 0.01$) for the YB₆ thin film with thickness of 100 nm. This estimate is larger than the value $\lambda_S(0) \approx 134$ nm measured by muon spin rotation study from a single crystal YB₆ sample³² with higher $T_c = 6.94$ K (and $2\Delta(0)/k_B T_c = 3.67$). This is reasonable considering that the higher T_c implies a longer mean free path l_{mfp} ,⁵⁸ and shorter $\lambda_S(0)$ through the relation $\lambda_S(0) = \lambda_L(0)\sqrt{1 + \xi_0/l_{mfp}}$ ⁵⁵ where $\lambda_L(0)$ is London penetration depth at $T = 0$ K and ξ_0 is BCS coherence length of the superconductor.

3. Validity of the extracted characteristic lengths of the SmB₆/YB₆ bilayers

To confirm the validity of the estimated values of the characteristic lengths of the SmB₆/YB₆ bilayers obtained in Sec. IV, one of the parameters ξ_N is converted to the Fermi velocity v_F , whose value has been reported from other measurements on SmB₆. From the clean limit relation $\xi_N = \hbar v_F / 2\pi k_B T$, one arrives at $v_F = 8.5 \times 10^4$ m/s. As seen from Table. II, this value is similar to the values obtained from the ARPES and DC transport measurements. However, the v_F values from theory and STM are an order of magnitude smaller. Recent DFT calculation accompanied by STM measurements^{59,60} and an independent theoretical calculation⁶¹ show that the discrepancy can be explained by termination-dependent band bending at the surface of SmB₆. The value of $\xi_N(2K)$ is also directly compared to that obtained from the DC transport study on Nb/SmB₆ bilayers.⁵⁶ The transport study has estimated a smaller value (9 nm) compared to our result (52 nm). This could be due to the differences in the grain size.

Appendix B: Dielectric resonator setup

The dielectric resonator setup was originally developed to study dielectric properties of materials⁴² and subsequently used to characterize microwave properties of high- T_c cuprate films.^{43,45,66} The comprehensive details of the dielectric resonator used in this work can be found in Ref.⁴⁴ Here, a summary of the key features is introduced for the reader's convenience. The resonator consists of a top and bottom metallic plate which confine the microwave field inside the resonator just as in a cavity (Fig. 5). A disk with high dielectric constant, which is placed on top of a superconducting thin film sample, concentrates the incident microwave fields injected from the excitation loop (p1 of Fig. 5) in the disk and generates a microwave resonance at certain frequencies f_0 . These resonant frequencies f_0 are determined mainly by the dimension and the dielectric constant of the disk. In our setup, a 3 mm diameter, 2 mm height rutile (TiO₂) disk is used as the dielectric disk. Rutile is chosen as the dielectric material for the resonator because it has very high dielectric constant ($\epsilon_c > 250$, $\epsilon_{a,b} > 120$ where a, b are the in-plane crystallographic axes and c is the out-of-plane axis) compared to those of sapphire ($\epsilon_{a,b,c} \sim 10$) or other dielectric materials. The high dielectric constant of the rutile helps to minimize the size of the disk, while maintaining the resonant frequencies in the microwave regime. The smaller the measurement area is, the more likely the sample will have homogeneous properties. Among the resonant modes generated by the dielectric resonator, the TE₀₁₁ mode (~ 11 GHz) induces a radial magnetic field and a circulating screening current on the sample surface. This circulating current helps to support the microwave transmission resonance. If there occurs any change of the sample properties such as superfluid density, that change can be studied through the change of the microwave transmission resonance. Note that the typical value of the quality factor of the TE₀₁₁ mode in this work is on the order of 10^4 . The simulated (HFSS) microwave magnetic field at the surface of the sample for the TE₀₁₁ mode is $\approx 8\mu T$ when the input microwave power P_{in} is -20 dBm. In this range of P_{in} , the resonance frequency does not show P_{in} dependence, showing that the sample is in the linear response regime in terms of the microwave magnetic field.

Appendix C: Measurement of the effective penetration depth

1. Determining resonance frequency and corresponding effective penetration depth

Microwave transmission data $S_{21}(f)$ near the resonance is fitted with the phase versus frequency fitting procedure,⁶⁷ to precisely determine the resonance frequency f_0 . Measurement and fitting of $S_{21}(f)$ data are repeated for different temperatures. From this, the tem-

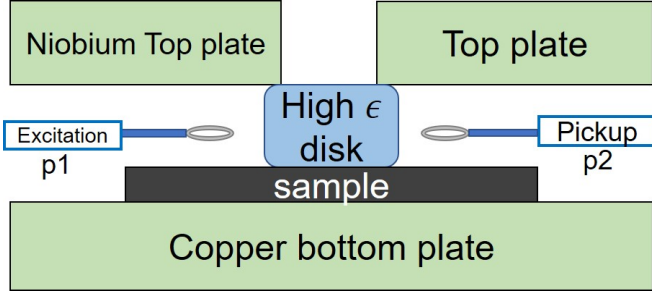


FIG. 5. Schematic cross-section diagram of the dielectric resonator setup for a microwave transmission resonance with a sample.

perature dependence $\Delta f_0(T) = f_0(T) - f_0(T_{ref})$ can be acquired. This temperature dependence of the resonance frequency can be converted to that of the effective penetration depth of a superconducting thin film sample by^{46,47,68}

$$\Delta\lambda_{eff}(T) = -\frac{G_{geo}}{\pi\mu_0} \frac{\Delta f_0(T)}{f_0^2(T)}. \quad (C1)$$

Here, $G_{geo} = \omega\mu_0 \int_V dV |H(x, y, z)|^2 / \int_S dS |H(x, y)|^2 = 225.3 \Omega$ is the geometric factor calculated numerically using the field solution inside the resonator for TE₀₁₁ mode derived by Hakki et al.⁴²

2. Determining error bars for the effective penetration depth and estimated fit parameters

The error bar in the effective penetration depth $\Delta\lambda_{eff}(T)$ is determined by the error bar of determination of the resonance frequency $f_0(T)$. The error bar of the f_0 is determined by a deviation of f_0 from the estimated value, which increases the root-mean-square error σ of the fit by 5%. The main source of the error bar of f_0 is the noise in $S_{21}(f)$ data. If the signal to noise ratio of S_{21} is large (small) which makes the $S_{21}(f)$ curve well- (poorly-) defined, f_0 can have a narrower (wider) range of values while giving fits with similar values of σ . Once the error bar of f_0 is determined, with the standard error propagation from the relation between $\Delta\lambda_{eff}(T)$ and $f_0(T)$, the error bar in the $\Delta\lambda_{eff}(T)$ data is estimated. The error bar for the estimated fit parameters ($\xi_N(T_0)$, $\lambda_N(0,0)$, and d_N) obtained from fitting $\Delta\lambda_{eff}(T)$ data are determined by a deviation from the estimated value which increases σ by 5%.

Appendix D: Further remarks on the electromagnetic screening model

1. Boundary conditions

Although explained in detail in Ref.,¹⁶ for the reader's convenience, the equation and the boundary conditions

for the magnetic field inside a proximity-coupled bilayer are described below. First, by combining Maxwell's equations with London's equation, one can obtain an equation for the tangential magnetic field for the bilayer

$$\frac{d^2 H(z)}{dz^2} + \frac{2}{\lambda_{N,S}(z)} \frac{d\lambda_{N,S}(z)}{dz} \frac{dH(z)}{dz} - \frac{1}{\lambda_{N,S}^2(z)} H(z) = 0. \quad (D1)$$

The boundary conditions for the tangential magnetic field for the geometry shown in Fig. 1 of the main article are as follows,

$$H(d_N) = H_0, \text{ (top surface)} \quad (D2)$$

$$H(-d_S) = 0, \text{ (bottom surface)} \quad (D3)$$

$$H(0^+) = H(0^-), \text{ (interface)} \quad (D4)$$

$$\lambda_N^2(0, T) \frac{dH(z)}{dz} \Big|_{z=0^+} = \lambda_S^2(0, T) \frac{dH(z)}{dz} \Big|_{z=0^-}, \quad (D5)$$

where $d_N \leq t_{SmB_6}$ is the proximity-coupled thickness of the normal layer and $d_S = t_{YB_6}$ is the thickness of the parent superconductor. The last boundary condition is a continuity condition for the superfluid velocity at the interface.

2. Field solutions

With Eq.(D1) and the approximated spatial profile of the induced order parameter in the normal layer $\Delta_N(z, T) = \Delta_N(0, T)e^{-z/\xi_N(T)}$ and the normal penetration depth $\lambda_N(z, T) = \lambda_N(0, T)e^{+z/\xi_N(T)}$, one can obtain the spatial profile of the magnetic field in the normal and superconducting layer as follows:¹⁶

$$H_N(z, T) = ApI_1(p) + BpK_1(p), \quad (0 \leq z \leq d_N) \quad (D6)$$

$$H_S(z, T) = Ce^{z/\lambda_S} + De^{-z/\lambda_S}, \quad (-d_S \leq z \leq 0), \quad (D7)$$

Here, the parameter p is defined as $p(z, T) = (\xi_N(T)/\lambda_N(z, T))e^{-z/\xi_N(T)}$ and I_1, K_1 are the modified Bessel functions of the first, second kind. The coefficients A, B, C, D can be calculated using the boundary conditions. The corresponding spatial profile of the current density can be obtained from z derivative of the magnetic field profile. After all the coefficients are obtained, the spatial profiles of the magnetic field and the current density of a normal/superconductor bilayer are fully determined. When calculating the inductance, the microwave loss is ignored so that the supercurrent density of the bilayer is approximated as the total current density $J_s \simeq J$. This is a valid approximation since the temperature range of the measurement (0~1.6 K) is well below T_c of the bilayer (~ 5.86 K) and the microwave photon energy (~ 0.044 meV) is much lower than the zero temperature superconducting gap of the YB₆ (> 1 meV).³²

- ¹ J. Alicea, Rep. Prog. Phys. **75**, 076501 (2012).
- ² C. Beenakker, Annu. Rev. Condens. Matter Phys **4**, 113 (2013).
- ³ A. Kitaev, Annals of Physics **321**, 2 (2006).
- ⁴ L. Fu and C. L. Kane, Phys. Rev. Lett. **100**, 096407 (2008).
- ⁵ N. Read and D. Green, Phys. Rev. B **61**, 10267 (2000).
- ⁶ D. A. Ivanov, Phys. Rev. Lett. **86**, 268 (2001).
- ⁷ A. Stern, F. von Oppen, and E. Mariani, Phys. Rev. B **70**, 205338 (2004).
- ⁸ M. Stone and S.-B. Chung, Phys. Rev. B **73**, 014505 (2006).
- ⁹ W. Dai, A. Richardella, R. Du, W. Zhao, X. Liu, C. X. Liu, S.-H. Huang, R. Sankar, F. Chou, N. Samarth, and Q. Li, Sci. Rep. **7**, 7631 (2017).
- ¹⁰ M.-X. Wang, C. Liu, J.-P. Xu, F. Yang, L. Miao, M.-Y. Yao, C. L. Gao, C. Shen, X. Ma, X. Chen, Z.-A. Xu, Y. Liu, S.-C. Zhang, D. Qian, J.-F. Jia, and Q.-K. Xue, Science **336**, 52 (2012).
- ¹¹ S.-Y. Xu, N. Alidoust, I. Belopolski, A. Richardella, C. Liu, M. Neupane, G. Bian, R. Huang, Song-Hsunand Sankar, C. Fang, B. Dellabetta, W. Dai, Q. Li, M. J. Gilbert, F. Chou, N. Samarth, and M. Z. Hasan, Nat. Phys. **10**, 943 (2014).
- ¹² J.-P. Xu, C. Liu, M.-X. Wang, J. Ge, Z.-L. Liu, X. Yang, Y. Chen, Y. Liu, Z.-A. Xu, C.-L. Gao, D. Qian, F.-C. Zhang, and J.-F. Jia, Phys. Rev. Lett. **112**, 217001 (2014).
- ¹³ J.-P. Xu, M.-X. Wang, Z. L. Liu, J.-F. Ge, X. Yang, C. Liu, Z. A. Xu, D. Guan, C. L. Gao, D. Qian, Y. Liu, Q.-H. Wang, F.-C. Zhang, Q.-K. Xue, and J.-F. Jia, Phys. Rev. Lett. **114**, 017001 (2015).
- ¹⁴ H.-H. Sun, K.-W. Zhang, L.-H. Hu, C. Li, G.-Y. Wang, H.-Y. Ma, Z.-A. Xu, C.-L. Gao, D.-D. Guan, Y.-Y. Li, C. Liu, D. Qian, Y. Zhou, L. Fu, S.-C. Li, F.-C. Zhang, and J.-F. Jia, Phys. Rev. Lett. **116**, 257003 (2016).
- ¹⁵ G. Deutscher and P. G. de Gennes, *Superconductivity*, Vol. 2 (Marcel Dekker, 1969) p. 1006.
- ¹⁶ M. S. Pambianchi, J. Mao, and S. M. Anlage, Phys. Rev. B **50**, 13659 (1994).
- ¹⁷ W. Belzig, C. Bruder, and G. Schön, Phys. Rev. B **53**, 5727 (1996).
- ¹⁸ P. G. de Gennes, *Superconductivity of Metals and Alloys* (Westview, 1999) p. 232.
- ¹⁹ J. Kim, Y.-J. Doh, K. Char, H. Doh, and H.-Y. Choi, Phys. Rev. B **71**, 214519 (2005).
- ²⁰ J. R. Hook, J. Low Temp. Phys. **23**, 645 (1976).
- ²¹ R. W. Simon and P. M. Chaikin, Phys. Rev. B **30**, 3750 (1984).
- ²² K. Kanoda, H. Mazaki, N. Hosoi, and T. Shinjo, Phys. Rev. B **35**, 8413 (1987).
- ²³ A. C. Mota, P. Visani, and A. Pollini, J. Low. Temp. Phys. **76**, 465 (1989).
- ²⁴ J. H. Claassen, J. E. Evetts, R. E. Somekh, and Z. H. Barber, Phys. Rev. B **44**, 9605 (1991).
- ²⁵ M. S. Pambianchi, S. N. Mao, and S. M. Anlage, Phys. Rev. B **52**, 4477 (1995).
- ²⁶ H. Onoe, A. Sumiyama, M. Nakagawa, and Y. Oda, J. Phys. Soc. Jpn. **64**, 2138 (1995).
- ²⁷ M. S. Pambianchi, L. Chen, and S. M. Anlage, Phys. Rev. B **54**, 3508 (1996).
- ²⁸ M. S. Pambianchi, C. Kwon, T. Venkatesan, and S. M. Anlage, Phys. Rev. B **54**, 15513 (1996).
- ²⁹ M. Cheng, R. M. Lutchyn, V. Galitski, and S. Das Sarma, Phys. Rev. B **82**, 094504 (2010).
- ³⁰ C. Kittel, *Introduction to Solid State Physics, 5th edition* (John Wiley and Sons, 2005) p. 268.
- ³¹ B. Clayman and R. Frindt, Solid State Commun. **9**, 1881 (1971).
- ³² R. Kadono, S. Kuroiwa, J. Akimitsu, A. Koda, K. Ohishi, W. Higemoto, and S. Otani, Phys. Rev. B **76**, 094501 (2007).
- ³³ A. Menth, E. Buehler, and T. H. Geballe, Phys. Rev. Lett. **22**, 295 (1969).
- ³⁴ N. Xu, P. K. Biswas, J. H. Dil, R. S. Dhaka, G. Landolt, S. Muff, C. E. Matt, X. Shi, N. C. Plumb, M. Radovic, E. Pomjakushina, K. Conder, A. Amato, S. V. Borisenko, R. Yu, H.-M. Weng, Z. Fang, X. Dai, J. Mesot, H. Ding, and M. Shi, Nat. Commun. **5**, 4566 (2014).
- ³⁵ P. Syers, D. Kim, M. S. Fuhrer, and J. Paglione, Phys. Rev. Lett. **114**, 096601 (2015).
- ³⁶ B. S. Tan, Y.-T. Hsu, B. Zeng, M. C. Hatnean, N. Harrison, Z. Zhu, M. Hartstein, M. Kiourlappou, A. Srivastava, M. D. Johannes, T. P. Murphy, J.-H. Park, L. Balicas, G. G. Lonzarich, G. Balakrishnan, and S. E. Sebastian, Science **349**, 287 (2015).
- ³⁷ N. J. Laurita, C. M. Morris, S. M. Koohpayeh, P. F. S. Rosa, W. A. Phelan, Z. Fisk, T. M. McQueen, and N. P. Armitage, Phys. Rev. B **94**, 165154 (2016).
- ³⁸ Y. Xu, S. Cui, J. K. Dong, D. Zhao, T. Wu, X. H. Chen, K. Sun, H. Yao, and S. Y. Li, Phys. Rev. Lett. **116**, 246403 (2016).
- ³⁹ J. Zhang, J. Yong, I. Takeuchi, R. L. Greene, and R. D. Averitt, Phys. Rev. B **97**, 155119 (2018).
- ⁴⁰ Y. S. Eo, A. Rakoski, J. Lucien, D. Mihailiov, C. Kurdak, P. F. S. Rosa, D.-J. Kim, and Z. Fisk, arxiv:1803.00959 .
- ⁴¹ S. Lee, V. Stanev, X. Zhang, J. Stasak, Drewand Flowers, J. S. Higgins, S. Dai, T. Blum, X. Pan, V. M. Yakovenko, J. Paglione, R. L. Greene, V. Galitski, and I. Takeuchi, Nature **570**, 344 (2019).
- ⁴² B. W. Hakki and P. D. Coleman, IEEE Trans. Microw. Theory Tech **8**, 402 (1960).
- ⁴³ J. Mazierska and R. Grabovickic, IEEE Trans. Appl. Supercond. **8**, 178 (1998).
- ⁴⁴ S. Bae, Y. Tan, A. P. Zhuravel, L. Zhang, S. Zeng, Y. Liu, T. A. Lograsso, Ariando, T. Venkatesan, and S. M. Anlage, Rev. Sci. Instrum. **90**, 043901 (2019).
- ⁴⁵ N. Klein, U. Dähne, U. Poppe, N. Tellmann, K. Urban, S. Orbach, S. Hensen, G. Müller, and H. Piel, J. Super. **5**, 195 (1992).
- ⁴⁶ B. B. Jin, N. Klein, W. N. Kang, H.-J. Kim, E.-M. Choi, S.-I. Lee, T. Dahm, and K. Maki, Phys. Rev. B **66**, 104521 (2002).
- ⁴⁷ R. J. Ormeno, A. Sibley, C. E. Gough, S. Sebastian, and I. R. Fisher, Phys. Rev. Lett. **88**, 047005 (2002).
- ⁴⁸ A. A. Abrikosov, *Fundamentals of the Theory of Metals* (Amsterdam: Elsevier, 1988) p. 364.
- ⁴⁹ R. Prozorov and R. W. Giannetta, Supercond. Sci. Technol. **19**, R41 (2006).
- ⁵⁰ M. I. Tsindlekht, V. M. Genkin, G. I. Leviev, I. Felner, O. Yuli, I. Asulin, O. Millo, M. A. Belogolovskii, and N. Y. Shitsevalova, Phys. Rev. B **78**, 024522 (2008).
- ⁵¹ N. E. Sluchanko, V. V. Glushkov, B. P. Gorshunov, S. V. Demishev, M. V. Kondrin, A. A. Pronin, A. A. Volkov,

- A. K. Savchenko, G. Grüner, Y. Bruynseraede, V. V. Moshchalkov, and S. Kunii, Phys. Rev. B **61**, 9906 (2000).
- ⁵² G. Deutscher, J. Hurault, and P. van Dalen, J. Phys. Chem. Solids. **30**, 509 (1969).
- ⁵³ R. W. Simon and P. M. Chaikin, Phys. Rev. B **23**, 4463 (1981).
- ⁵⁴ D. S. Falk, Phys. Rev. **132**, 1576 (1963).
- ⁵⁵ M. Tinkham, *Introduction to Superconductivity, 2nd edition* (Dover publications, Inc., 1996) p. 97.
- ⁵⁶ S. Lee, X. Zhang, Y. Liang, S. W. Fackler, J. Yong, X. Wang, J. Paglione, R. L. Greene, and I. Takeuchi, Phys. Rev. X **6**, 031031 (2016).
- ⁵⁷ J. Yong, Y. Jiang, D. Usanmaz, S. Curtarolo, X. Zhang, L. Li, X. Pan, J. Shin, I. Takeuchi, and R. L. Greene, Appl. Phys. Lett. **105**, 222403 (2014).
- ⁵⁸ N. Sluchanko, V. Glushkov, S. Demishev, A. Azarevich, M. Anisimov, A. Bogach, V. Voronov, S. Gavrilkin, K. Mitsen, A. Kuznetsov, I. Sannikov, N. Shitsevalova, V. Filipov, M. Kondrin, S. Gabáni, and K. Flachbart, Phys. Rev. B **96**, 144501 (2017).
- ⁵⁹ H. Pirie, Y. Liu, A. Soumyanarayanan, P. Chen, Y. He, M. M. Yee, P. F. S. Rosa, J. D. Thompson, D.-J. Kim, Z. Fisk, X. Wang, J. Paglione, D. K. Morr, M. H. Hamidian, and J. E. Hoffman, arXiv:1810.13419 .
- ⁶⁰ C. E. Matt, H. Pirie, A. Soumyanarayanan, M. M. Yee, Y. He, D. T. Larson, W. S. Paz, J. Palacios, M. Hamidian, and J. E. Hoffman, arXiv:1810.13442 .
- ⁶¹ V. Alexandrov, P. Coleman, and O. Erten, Phys. Rev. Lett. **114**, 177202 (2015).
- ⁶² M. Neupane, N. Alidoust, S.-Y. Xu, T. Kondo, Y. Ishida, D. J. Kim, C. Liu, I. Belopolski, Y. J. Jo, T.-R. Chang, H.-T. Jeng, T. Durakiewicz, L. Balicas, H. Lin, A. Bansil, S. Shin, Z. Fisk, and M. Z. Hasan, Nat. Commun. **4**, 2991 (2013).
- ⁶³ J. Jiang, S. Li, T. Zhang, Z. Sun, F. Chen, Z. R. Ye, M. Xu, Q. Q. Ge, S. Y. Tan, X. H. Niu, M. Xia, B. P. Xie, Y. F. Li, X. H. Chen, H. H. Wen, and D. L. Feng, Nat. Commun. **4**, 3010 (2013).
- ⁶⁴ B. Roy, J. D. Sau, M. Dzero, and V. Galitski, Phys. Rev. B **90**, 155314 (2014).
- ⁶⁵ T. Liu, Y. Li, L. Gu, J. Ding, H. Chang, P. A. P. Janantha, B. Kalinikos, V. Novosad, A. Hoffmann, R. Wu, C. L. Chien, and M. Wu, Phys. Rev. Lett. **120**, 207206 (2018).
- ⁶⁶ N. Pompeo, R. Marcon, and E. Silva, Journal of Superconductivity and Novel Magnetism **20**, 71 (2007).
- ⁶⁷ P. J. Petersan and S. M. Anlage, J. Appl. Phys. **84**, 3392 (1998).
- ⁶⁸ M. A. Hein, *High-Temperature Superconductor Thin Films at Microwave Frequencies* (Springer, Heidelberg, 1999) pp. 45–46.